ORIGINAL RESEARCH ARTICLE

The Influence of Powder Reuse on the Properties of Nickel Super Alloy ATI 718™ in Laser Powder Bed Fusion Additive Manufacturing

CHRISTOPHER ROCK, CHRISTOPHER LEDFORD, MATIAS GARCIA-AVILA, HARVEY WEST, VICTORIA M. MILLER, MARK PANKOW, RYAN DEHOFF, and TIM HORN

Gas-atomized nickel alloy ATI 718™ powders with a nominal particle distribution of 15 to 45 μm were used in a laser powder bed fusion (LPBF) additive manufacturing (AM) process for ten sequential builds without refreshing with new powder. The repeated feedstock use caused the particle size distribution, particle morphology, and oxygen content to change in comparison to virgin powder. Unusual particle morphologies were observed in the powder with repeated use when compared to virgin gas-atomized feedstock. Particles after use were found to contain surface features such as films and spots, which consisted of aluminum oxides and likely contributed to increasing the oxygen content in the recycled feedstock powder.

https://doi.org/10.1007/s11663-020-02040-2
© The Minerals, Metals & Materials Society and ASM International 2021

I. INTRODUCTION

METALLIC powder feedstocks are often reused or recycled in powder bed fusion (PBF) additive manufacturing (AM) processes due to high powder cost and limited availability.[1,2] Typically, after each build, non-consolidated powders are collected, screened to under 53 μm, and placed back into the feeder chamber for reuse in the next build. Depending on the part size and application, virgin powder is often blended with used powder before each build. This makes traceability and qualification of the powder feedstock and parts produced by AM very difficult if the blended powders have different properties and use conditions. If spatter particles exist either in the recycled powder or are generated during the process and become melted by the laser or electron beam (EB) in PBF and get incorporated into the part, traceability becomes especially challenging.

While many papers have been published on feedstock reuse and recycling in PBF, test articles are typically samples or blocks designed for metallurgical or static mechanical testing studies. Sample layouts such as this do not always represent a tightly packed build, where the reported effects of powder recycling on powder and part properties are generally mixed.[3–7] Tang *et al.* and Nandwana *et al.* studied the recyclability of powders used in the Arcam EB process.[3,4] Tang *et al.* reported an increase in oxygen content from 0.08 to 0.19 wt pct during recycling Ti-6Al-4V powder 21 times in an EB machine producing a minimum of six 8 mm diameter samples per build.[3] The study also reported an increase in yield strength and ultimate tensile strength with powder reuse. Nandwana *et al.* studied the effect of recycling Ti-6Al-4V and 718 powders in an Arcam EB process by reusing the feedstock 5 and 6 times, respectively, without refreshing with new powder.[4] The oxygen content of 718 powders increased slightly between builds 1 and 6, after consecutive reuse, whereas Ti-6Al-4V was more susceptible to oxygen pickup. The oxygen increase in Ti-6Al-4V was attributed to moisture pickup during machine changeover and powder handling where water adsorbed onto the powder surfaces disassociated at high temperature such as bed preheat

CHRISTOPHER ROCK, CHRISTOPHER LEDFORD, and HARVEY WEST are with the Center for Additive Manufacturing and Logistics, North Carolina State University, Campus Box 7906, Raleigh, NC 27695-7906. MATIAS GARCIA-AVILA is with the ATI Specialty Materials, 2020 Ashcraft Ave., Monroe, NC 28110. VICTORIA M. MILLER is with the Department of Materials Science and Engineering, University of Florida, 100 Rhines Hall, Gainesville, FL 32611. MARK PANKOW is with the Department of Mechanical and Aerospace Engineering, North Carolina State University, Campus Box 7910, Raleigh, NC 27695-7910. RYAN DEHOFF is with the Manufacturing Demonstration Facility, Oak Ridge National Laboratory, Knoxville, TN 37932 and also with the Materials Science and Technology Division, Oak Ridge National Laboratory, Knoxville, TN 37831. TIM HORN is with the Center for Additive Manufacturing and Logistics, North Carolina State University and also with the Department of Mechanical and Aerospace Engineering, North Carolina State University. Contact e-mail: tjhorn@ncsu.edu

Manuscript submitted February 20, 2020; Accepted November 10, 2020.

Article published online January 6, 2021.

and increased the oxygen content in the powder.[4] Also, each alloy experienced a small increase in average particle size, due in part to the use of the Arcam powder recovery system, which preferentially removes fines upon recycling. In general, it was concluded that alloy 718 was less affected by powder reuse compared to Ti-6Al-4V. Ardila *et al.* studied the microstructure and mechanical properties of test coupons fabricated with laser PBF using 718 powder. They reported no significant changes in powder characteristics or mechanical properties after 14 reuse cycles.[5] This study screened the used powder through a 63 μm screen after each use to remove any spatter or bed particles which may have interacted with the melt pool or plume. Although no significant changes were reported in the particle characteristics and solid samples, no data on oxygen content were published, so the influence of oxidation on composition during recycling is unknown.[5]

Slotwinski *et al.* studied 17-4 stainless steel (SS) powders by recycling them eight times in laser PBF and screening through an 80 μm sieve where an increase in particle size distribution (PSD) was observed with reuse.[6] The screened residual particles showed unusual morphologies, an increase in BCC phase, and X-ray photoelectron spectroscopy (XPS) identified iron oxidation on the particle surfaces. However, the − 80 μm screened and recycled powder showed little effect of reuse. In a continuation study by Jacob *et al.*, the physical properties of S17-4PH powder and solid samples were characterized after recycling. It was reported that no significant changes were observed in the properties of the recycled powder and fabricated solids samples (chemical composition, mechanical properties, density, hardness) after 11 reuses, although oxygen was not reported.[7] It was observed that changes in particle behavior such as flowability and an increase in BCC phases in the solids were observed with the reuse of powder. Strondtl *et al.* studied powder behavior in laser PBF by recycling, screening residual powder, and blending with virgin powder.[8] This study reported that the powder experienced increased flowability during recycling by fines removal during part production. An increase in fabricated part porosity was also observed and was associated with the removal of fines, which help fill interstitial positions in a particle distribution and aid densification. Additionally, ductility decreased, and oxygen increased as a result of recycling powder in mechanical samples tested.[8]

Simonelli *et al.*[9] studied spatter generated SS 316L, Al-Si10-Mg, and Ti-6Al-4V by laser PBF processes by screening used powder and analyzing on-screen residual particles larger than virgin powder. This research used SEM and EDS to show the presence of surface oxide contamination on screened residuals consisting mainly of Si, Mn, and Mg not observed on virgin SS316L powder. Other recent studies have found similar oxidized particle surfaces and spots in a variety of alloy systems[9–12] where the oxides appear to form from low free energy oxide-forming elements such as Ti, Si, and Al when present in the alloy.

These studies and general industry practices suggest that a common notion in PBF feedstock reuse is that screening to near the maximum size of the virgin powder PSD removes spatter, agglomerates, oxides, metallic slivers or other features, which are artifacts of the laser PBF process. The critical assumption is that interacted feedstock or process-generated particles, such as spatter, are typically larger than the starting PSD and are entirely screened out before reuse. However, this practice ignores two observed phenomena; first, that spatter particles, ejecta, and agglomerates often land adjacent to the melt track or become ejected around the build chamber and are candidates for incorporation into a part. Second, smaller entrained particles which do not necessarily change size may be affected through interaction with the laser, plasma plume, high temperatures, or ambient atmosphere,[13,14] and can pass through a screen. Therefore, although screening oversized particles during recycling is an essential part of the process, it does not necessarily remove all affected particles, which may become incorporated into parts.

The available literature also tends to present results in terms of the number of recycling events without context regarding build geometry, laser path length, or the root cause of the observed changes in powder characteristics. In the current study, the component geometry and toolpath were calculated to target a beam scan line length per layer to generate as much spatter as possible using standard parameters within the machine build area (250 mm × 250 mm), and powder capacity (200 kg) limitations to mimic a full build area. The study was designed to explore an extreme scenario for powder reuse and examines the effect of process-generated spatter and laser-interacted particles. The powder was reused without refreshing the batch with new powder and only screened with an oversized (140 mesh) screen to remove excessively large particles such as agglomerates that would otherwise inhibit powder bed formation. This approach allowed for the generation and retention of a significant amount of spatter and particles that had interacted with the virgin gas-atomized (GA) powder during ten reuse events. These powder particles were characterized for change in physical properties such as flow, composition, and morphology.

II. EXPERIMENTS AND METHODOLOGY

Approximately 200 kg of virgin GA nickel super alloy ATI 718™ powder was used in this study after screening to a 15 to 45 μm nominal PSD. From this powder, ten consecutive test articles (blocks) measuring 127 mm × 127 mm in area and of diminishing height were fabricated using an EOS M280 PBF system. The test article was rotated − 15 deg about the *z*-axis and fabricated on a standard steel build substrate. The OEM parameter set for IN718_Surface was used with 20 μm layer thickness (EOS RP-Tools_6_2_13). The chamber was purged with argon gas (99.97 pct purity) to keep oxygen below 0.1 pct during fabrication and flow rate of 100 L/min.

The size and shape of the blocks were selected to maximize both the amount of incident spatter and ejecta based on preliminary experiments to maximize the number of possible spatter in samples (*i.e.,* spatter and ejecta that lands in the path of a subsequent melt track). The dimensions were constrained to accommodate harvesting sub-size (ASTM E8) vertical and horizontal tensile and fatigue specimens from a number of recycled blocks subject to the suitable build heights, especially for any vertical test samples. The final (10th) build was 12 mm tall, enough to potentially extract horizontal mechanical samples, and it was determined that no further samples were possible from future builds due to the block height.

Starting with the PBF fabrication of the first test article, the experimental sequence and methodology were as follows: Approximately 200 kg of as-received ATI 718™ powders were blended in a rotary drum for 30 minutes at 4 RPM and loaded into the collection chamber. Powder samples were taken from the collection chamber (150 to 200 g) prior to the first build using an ASTM B215-15 powder sample thief and methodology. The test article was fabricated using the methodology and parameters described previously until the powder in the deposition tank was exhausted.

Powder samples (100 to 150 g) were then collected from different locations in the build chamber after each iteration, as described in Figure 1(b), repeating the ASTM B215-15 protocol for powder sampling with a powder thief. Samples were labeled and stored in sealed glass vials for analysis. Samples taken from horizontal surfaces in the chamber outside the bed area, such as powder ejected onto the Argon Duct in Figure 1(b) were collected directly into a sample vial without the use of a powder thief and were random in weight based on the amount available for collection up to a maximum of 50 g.

All powders were then removed from the machine and placed in a 100-L, 304 stainless steel drum. Powder from the collector container and powder from the build platform were blended together in the stainless steel drum for 30 minutes at 4 RPM. This post-build blended powder was sampled and sieved through a 140 mesh screen (105 μm mesh size). The 140 mesh screen was chosen to test a condition intended to mimic larger spatter particles stochastically landing in the bed and provide a 'worst case scenario' with the intention of understanding the effects of spatter and powder reuse on the feedstock during part melting yet maintaining the ability to separate heavily agglomerated particles and debris or contamination introduced during the process that may interrupt subsequent powder bed formation. From a practical standpoint, and preliminary trials, 140 mesh was the largest permissible particle size that would still produce solid samples without a high risk of catastrophic build failure (*e.g.,* delamination or curling blocking or damaging the powder spreader) within the parameter window defined in this study. The − 140 mesh screened powder was then sampled and loaded back into the EOS M280 dispenser chamber for the next iteration while the +140 mesh particles were retained for analysis. A new build substrate was installed and the process was repeated for a total of 10 builds. Figure 2 shows the first 6 out of total 10 as-built test articles. With each subsequent build, the article height trended down as illustrated in Figure 2, which was solely determined by the amount of reused powders remaining for each build.

From each dispenser powder sample, several measurements were carried out. PSD was determined using laser diffraction (ASTM B822-17, Microtrac S3500). The analysis was carried out in deionized water, with Triton X-100 surfactant and ultrasonic agitation. Data were recorded for both volumetric and number distributions. Powder flowability was measured *via* a calibrated mass Hall Flowmeter (ASTM B213-13) in an environmental chamber at 21 °C and 30 pct relative humidity. Scanning electron microscopy (SEM) with secondary electron imaging (SEI) and backscatter elemental composition (BEC) detectors and energy-dispersive spectroscopy (EDS) was carried out to characterize powder morphology and surface chemistry on a JEOL JSM-6101LA. Chemical analyses were conducted by inert gas fusion and inductively coupled plasma mass spectroscopy (ICP). Magnetic coercivity was measured on a SQUID by Quantum Design MPMS3. It should be noted that while all powder samples were analyzed for at least PSD and SEM for morphology, the scope of this report focuses on the characterization of powder used to make the builds after screening; therefore, the full powder analysis was performed using virgin powder and − 140 mesh screened (recycled) powder. SEM, EDS, and oxygen content of selected spatter samples are also mentioned in the report as a comparison to dispenser powder used to perform the builds.

In addition to the ATI 718™ powders used for the bulk of the study, commercially obtained 316L and Co28Cr6Mo powders were used only as alternative examples of spatter. The general chemistry of all three alloys is shown in Table I.

III. RESULTS AND DISCUSSION

Figure 3 and Table II show the volumetric PSD of the dispenser powder feedstock over the course of the consecutive builds. The nomenclature in Figure 3 represents the powder prior to its accompanying build (*i.e.*, pre-1 is virgin powder whereas pre-10 has been used 9 times). The data in Figure 3 show that the PSD curve flattened as its volumetric d_{50} increased slightly from 35 μm in virgin powder to 40 μm prior to the tenth build; however, large changes were not observed in the median particle size. A noticeable change in PSD occurs after 140 mesh screening where the curves widen with number of reuses as the population of particles greater than 45 microns increases. This is demonstrated in Table II by examining the d_{90} particle size that increase from 49 to 85 μm in the dispenser feedstock prior to the tenth build.

Naturally, the PSD widens after screening powder through a screen larger than 45 μm. However, that strongly indicates that the process is generating and accumulating larger particles, most likely from the melt pool and particle interactions,[13,14] which become

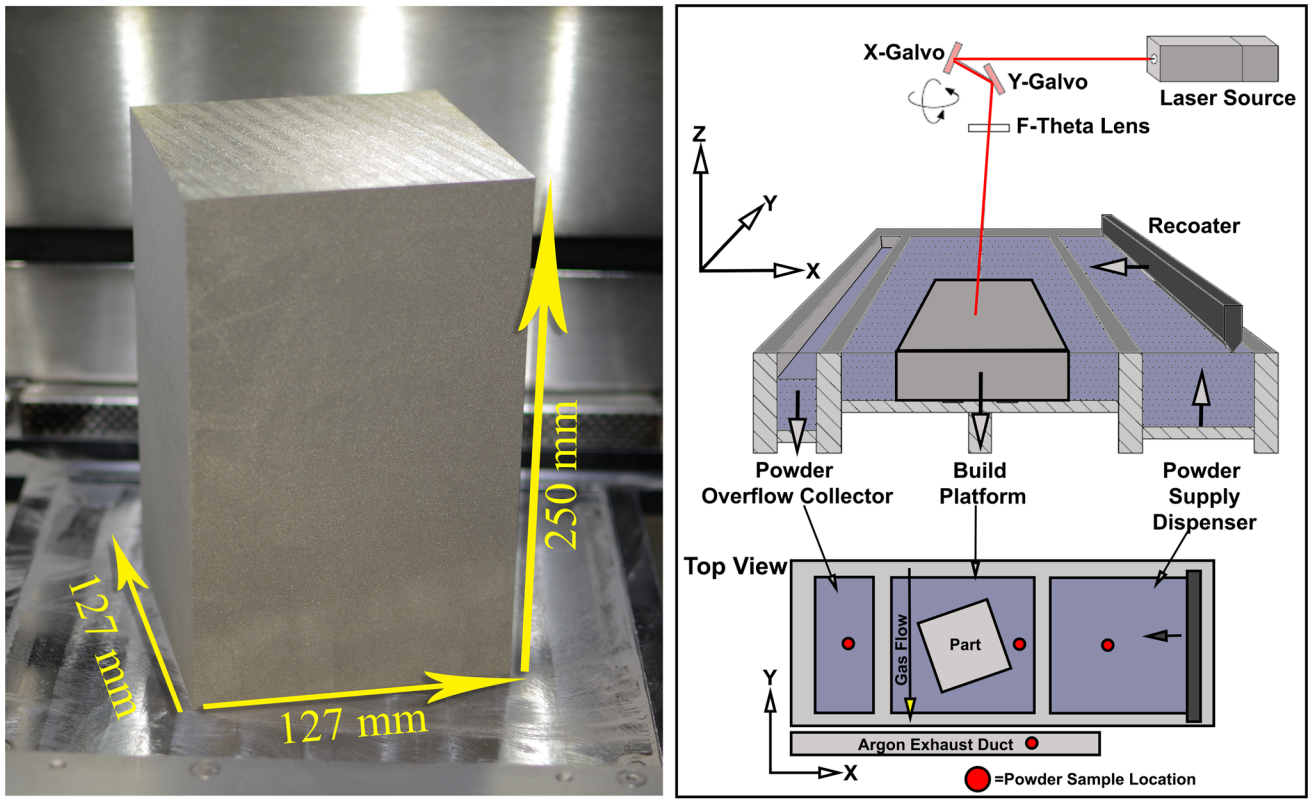

Fig. 1—(*a*) An image of the maximum size (127 mm × 127mm × 204 mm) block printed in this study, (*b*) schematic of the build tank and sample location.

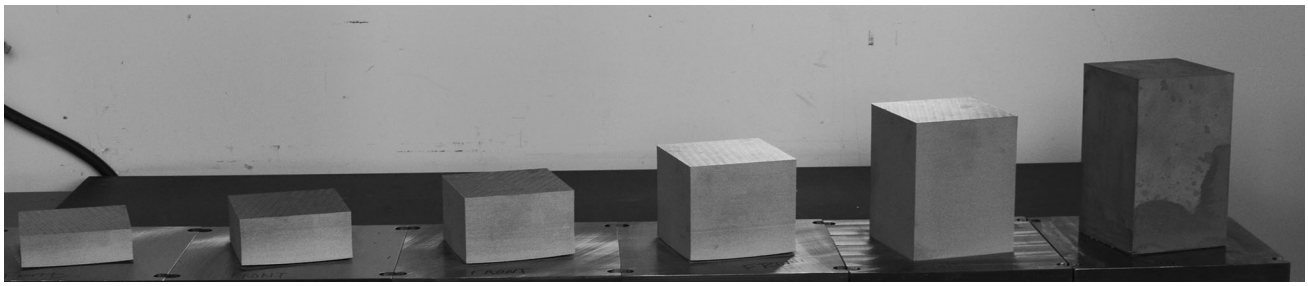

Fig. 2—Six of the ten blocks produced in the recyclability study in an EOS M280 from build 1 to build 6 (right to left) to demonstrate the block height decrease by reusing powder without refreshing.

intimately mixed with the powder. While many of the coarser particles can be screened out in post-processing with a finer mesh screen, these data show that many of the particles generated are ejected into the surrounding bed with the possibility of being incorporated into the laser melt path and, subsequently, into the part, especially on heavily packed build areas. Figures 4(a) through (c) illustrate the effect of PSD coarsening on the performance of the recycled powders. Figure 4(a) plots the diverging slopes of the median and maximum (d_{50} and d_{90}, respectively) PSD measured over the course of the study, and Figure 4(b) tracks powder flowability with reuse.

The curves in Figure 4(a) show particle coarsening in the size distribution, especially in the 90th percentile of the distribution, while the median exhibits a slight increase over the duration of the study and indicates the generation and increasing accumulation of coarse particles back into the powder during reuse. Figure 4(b) illustrates the increase in Hall flow time with the number of times reused and subsequent coarsening PSD where the time to flow increased linearly from 11.3 s/50 g with virgin powder to 13.5 s/50 g after ten uses. Figure 4(c) also shows the effect of particle coarsening on flowability by evaluating the effect of d_{90} particle size on the Hall flow rate over the course of the study and demonstrates

Table I. Typical Chemical Composition (Wt Pct) for 718, 316L, and Co28Cr6Mo Powders

Alloy	Ref.	C	Mn	Si	P	S	Cr	Co	Mo	Nb + Ta	Ti	Al	Fe	Ni
718	15	0.08*	0.35*	0.35*	0.015*	0.015*	17 to 21	1.0*	2.8 to 3.3	4.75 to 5.50	0.65 to 1.15	0.2 to 0.8	—	50 to 55
316L	16	0.03*	2.0*	1.0*	0.045*	0.030*	16 to 18	—	2.0 to 3.0	—	—	—	Bal.	10 to 14
CoCrMo	17	0.35*	1.00*	1.00*	0.020*	0.010*	27.00 to 30.00	bal	5.00 to 7.00	—	0.10*	0.10*	0.75*	0.50*

*Maximum allowed.

that as the d_{90} of − 140 mesh recycled powder increases, the Hall flow times increase by accumulating larger particles during use.

Typically, for a given powder system with similar properties and environmental conditions, coarse powder flow times are lower for a given alloy system than fine powder distributions for particles in this size range. However, the reverse was consistently observed during this study, suggesting other factors are influencing the flow properties in these recycled powders. While the Hall flow test is a fairly good indicator for batch flow characteristics of a particulate system, especially with spherical particles, it is rather insensitive to other factors that may influence cohesion.[18] Characteristics such as moisture, morphology, particle surface roughness, bimodal distributions, or attached satellites, among others, can significantly influence measured flow times[18] in part because of the simplicity of the test.

Morphological changes due to the introduction of coarse powders during recycling were observed by SEM before and after screening each build cycle. Figures 5(a) through (c) show typical SEM images of the − 140 mesh powder pre-build 1, 5, and 10, respectively, where Figure 5(a) morphologies are typical of the virgin GA powder. However, after multiple uses and screening through a − 140 mesh screen, larger particles are observed in the distributions (Figures 5(b) and (c)), and the observed increase in the proportion of these larger particles was consistent with laser diffraction PSD measurements. The larger particles were observed to contain a mix of highly spherical and non-spherical (ovoid, oblong, and agglomerates/satellites) morphologies, which appeared to influence batch flow as increasing numbers of larger particles were introduced into the distribution. As the powder across all samples was environmentally conditioned prior to testing, it is expected that the reduction in flowability is due in large part to the increasingly bimodal distribution of the feedstock where the smaller atomized particles become candidates for interstitial particle friction with the introduced larger particles. Also, many of the larger particles had non-spherical agglomerated or fused particle morphologies, which also contributed to increasing Hall flow times. From a practical perspective, while the flow time was shown to increase, no noticeable spreading issues were observed in the EOS M280 until runs 9 and 10, where so many large and unusually shaped particles began to cause streaking and other bed-related issues.

The oxygen content of the reused powder was measured by inert gas fusion (LECO OH836) after screening at − 140 mesh, and prior to loading back into the machine. Figure 6 shows the weight pct of oxygen in the powder plotted against build iteration and demonstrates that the oxygen nearly doubled in content during the study. The starting 718 powder contained 130 ppm oxygen, while the powder used in the final iteration contained 230 ppm oxygen content. The oxygen content of spatter collected in the machine away from the build area was also measured after selected builds and ranged from 180 ppm up to a maximum value of 280 ppm. Figure 6 examines the influence of oxygen content on

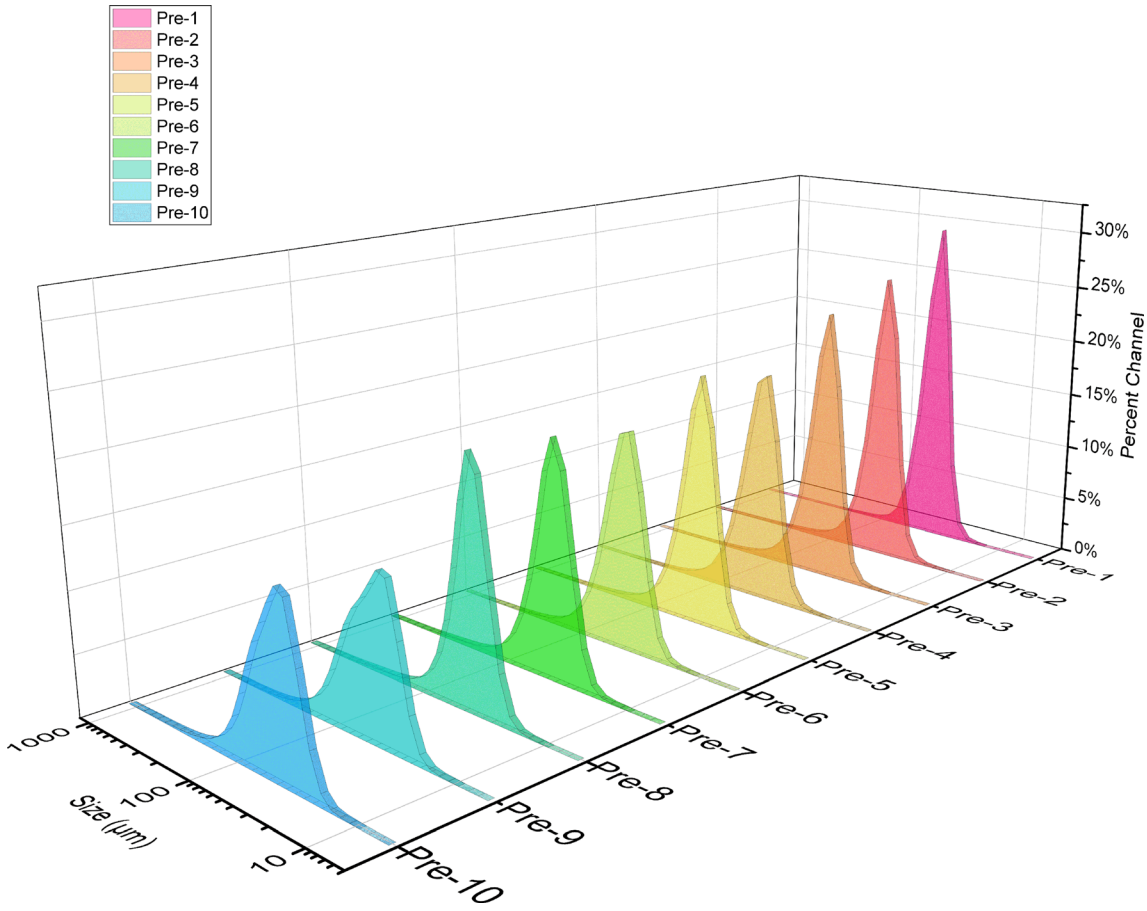

Fig. 3—Influence of powder reuse on particle size distribution in 718 powder used repeatedly in EOS M280; screened through − 140 mesh screen. Nomenclature: (Pre-1, 15 to 45 μm), Pre-6 (feedstock after 5 uses), and Pre-10 (feedstock after 9 uses).

Table II. Volume Particle Size Distribution Percentiles d_{10}, d_{50}, d_{90} for Recycled Powders

Sample	d_{10} (μm)	d_{50} (μm)	d_{90} (μm)
Pre-1	26.5	31.5	49.3
Pre-2	25.5	34.9	54.4
Pre-3	26.3	36.7	60.6
Pre-4	26.6	39.2	67.9
Pre-5	25.4	36.8	63.6
Pre-6	26.5	40.1	72.3
Pre-7	24.5	36.5	66.8
Pre-8	25.4	39.4	75.3
Pre-9	24.6	42.3	93.5
Pre-10	24.3	40.2	84.6

the powder after reuse of up to ten times. The black-filled symbols in Figure 6 represent the oxygen content of − 140 mesh powder feedstock used during the 10 builds just prior to producing the test articles. Samples of the − 140 mesh powder were also screened to − 325 mesh (not used in the builds) to separate the particles greater than and equal to the starting atomized powder for the purposes of oxygen analysis. Figure 6 shows that the larger particles generated during PBF (+325/− 140: open circle symbols) have an elevated oxygen content compared with both the − 140 mesh powder and − 325 mesh powder and increase significantly with usage. It is clear that as particles larger than 45 μm are added to the system during laser PBF, the oxygen increases substantially where the larger particles (+325/− 140 mesh) are strongly influenced by the process and residual oxygen contamination in the inert machine atmosphere. Usually, finer powder has higher oxygen content compared with coarser powders for a given condition due to the influence of the oxide film compared with bulk volume. The larger particles here are formed initially as liquid spatter by either ejection from the melt pool or from various interactions of entrained bed powder.[13] Therefore, as the larger spatter particles increase in population over the course of this study, their effect on the powder system increases the oxygen in the feedstock during usage by melting multiple times, each time with an increasing number of high oxygen spatter particles, incrementally increase oxygen in the system after each reuse. Therefore, the data in Figure 6 show that the coarse powder ejecta not only influences flowability (Figure 4(b)) but also increases the oxygen content of the powder system when not completely removed.

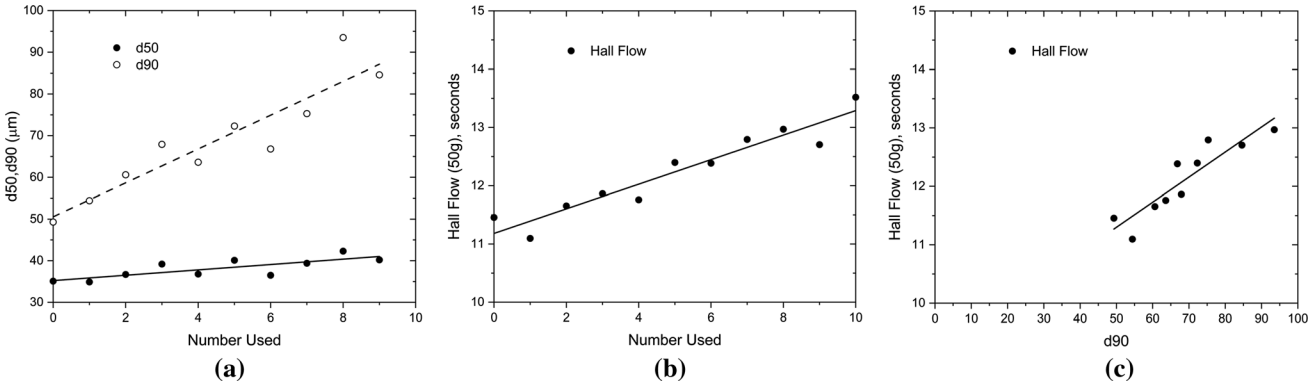

Fig. 4—Effect of powder reuse on (*a*) d_{50}, median particle size distribution, d_{90} percentile particle size, (*b*) Hall flow, and (*c*) effect of d_{90} on Hall flow.

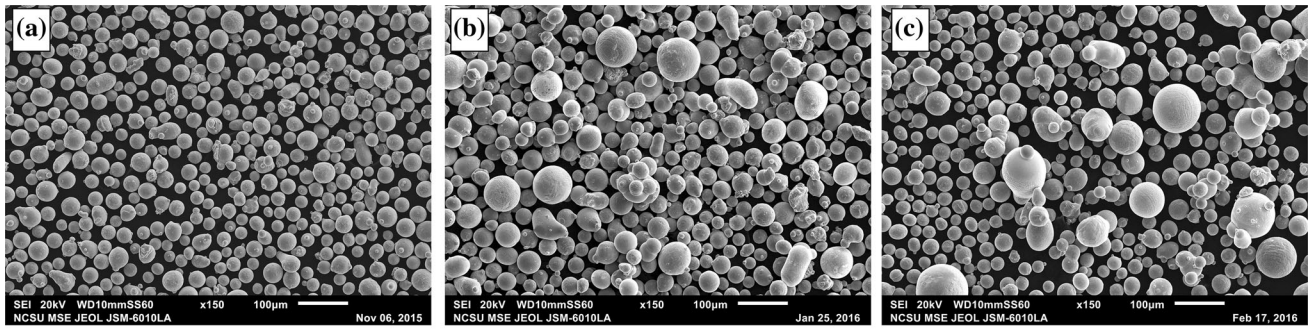

Pre Build #1 (Initial build)
D50= 35μm

Pre Build #6
D50= 40μm

Pre Build #10
D50= 40μm

Fig. 5—SEM images showing changes in particle size and morphology with increasing use and screening through − 140 mesh screen. The as-received powder, prior to the first build is shown in (*a*), powder prior to the 6th build is shown in (*b*) and powder prior to the 10th build is shown in (*c*). Note all scale bars and magnifications are the same for each image.

Another observation in Figure 6 is that the − 325 mesh bed powder demonstrated a small increase in oxygen content during the study from 140 ppm to a maximum value of 180 ppm. This most likely is due to entrainment and interaction of localized bed powder with the melt area during the build process. Recent studies [13,14] combining modeling and high-speed videos clearly demonstrate that some local bed powder interacts with the melt area and plume, causing selected entrained bed particles to become dislodged, heated, and in some instances, melted during the process. This entrainment phenomenon could be the reason for − 325 mesh particles to slowly gain oxygen during reuse while not necessarily remelting.

Most of the larger spatter particles generated dynamically during melting can be screened out in offline processes. However, during part making, these larger, high oxygen content larger particles (+ 325/− 140 mesh) can become candidates for melting and incorporation into a part if ejected into the subsequent beam path. Therefore, it is very important to characterize the general spatter morphologies and features to distinguish them from the well-known properties of virgin atomized powder. To start, repeated morphological particle comparisons were performed on powder samples collected from all builds to explore observable reuse effects and develop a compendium of particle morphologies observed during recycling under these extreme conditions. It should be noted that chemistry examinations of the major elements by ICP showed no change in recycled powders during this study, including Al and Ti, which indicates that rather than evaporating, these elements tend to form oxides leading to the increase in oxygen, especially by the coarser, ejected powder particles in the imperfect, but low oxygen atmosphere of the build chamber.

Figures 7(a) through (d) are SEM images of the most commonly observed morphological features in the present batch of GA 718 powder and is representative of GA powder of similar compositions.[19,20] Figure 7(a) shows the most common morphology observed in the feedstock where most of the particles were reasonably spherical with a combination of smooth and slightly dimpled surfaces common in GA powders of similar compositions. Other commonly observed morphologies shown in Figures 7(b) through (d) are liquid accretion particles (Figure 7(b)) most likely formed by a solid particle colliding with liquid ligaments or liquid spheres

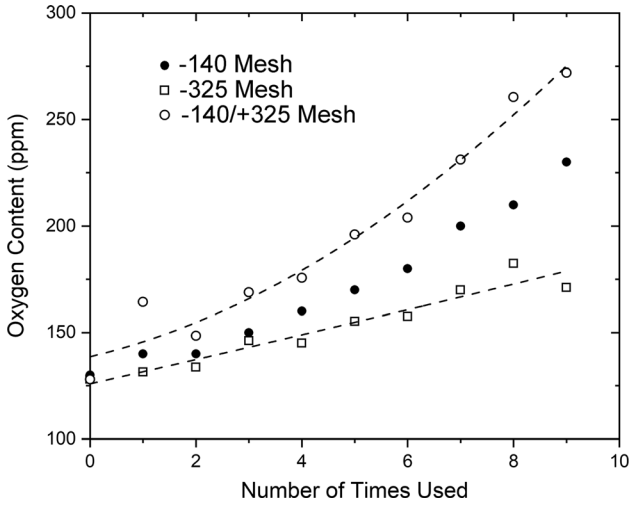

Fig. 6—Effect of powder reuse on oxygen content in − 140 mesh powder. Symbols used in the graph are pre-run powder for each time used (filled circle), pre-run powder screened to − 325 (open rectangle), and pre-run powder screened to − 140 + 325 mesh (open circle).

during atomization, ovals (Figure 7(c)) that solidified prior to pinching into a spherical particle(s), and particles with attached satellites (Figure 7(d)).

In contrast to gas atomization particle morphologies, Figures 8(a) through (d) show commonly observed spatter particles collected during the recyclability experiment. Figure 8(a) shows the most commonly observed spatter particle during the study, a highly spherical and satellite-free dendritic spatter particle. These particles commonly have very high sphericity and are absent of interaction-based surface features such as satellites or dimples, indicating these particles have time to form and solidify outside of the turbulent melt pool area and associated entrained particles. These particles were found in nearly every collected sample throughout the study except in the virgin GA powder feedstock. Figure 8(b) is a similarly spherical, dendritic particle that is covered with a surface film morphologically different from the liquid accretion GA particle observed in Figure 7(b). Figure 8(c) shows another morphology different from the virgin GA powder used in this study where multiple GA particles are agglomerated by a liquid ligament-forming compression features on its surface and are expected that this agglomeration is the result of entrained bed particles interacting with a liquid ligament ejected from the melt pool. Figure 8(d) demonstrates a mixed morphology particle common to 718 spatter found in this study where a highly dendritic particle is combined with liquid ligament forming a cap with a third particle lodged into the top. The morphologies in Figures 8(c) and (d) appear to be a combination of spatter and entrained bed particle(s) conjoined together. A recent report by Ly *et al.*[13] found that a portion of spatter is entrained bed particles, dislodged by fluid dynamics and vapor effects associated with the extreme localized temperatures of the melt area during AM. Others have reported particles with morphologies atypical of GA powders after PBF in 718 and similar alloy systems such as 316L and 718, among others.[9–11,21–26] These morphologies are most likely formed during the collision of liquid ejection from the melt pool and particle entrainment, which interacts in the extreme and localized chaotic environment of the plume and melt pool.[10,11,24–27] While Figures 8(a) through (d) are common examples of typical spatter morphologies observed, many different combinations were seen over the course of the study.

External spots, films, and blisters were also commonly observed on particles throughout this study, and examples of SEM secondary (SEI) and backscatter composition (BEC) modes of three particles illustrating these features are shown in Figure 9. The blisters and selected surface films of the particles shown in Figure 9 did not demonstrate noticeable composition differences between SEI and BEC modes. However, the SEM may not be sensitive enough to detect composition differences in thin surface films due to beam interaction volume and most likely needs a more sensitive characterization approach. The particle in Figure 9(d) indicated light element-rich spots from the BEC detector. Since localized compositions in this alloy system are important for maintaining properties and avoiding defects, these particle features are of great interest. Recent reports on recyclability, melt pool, and spatter studies have demonstrated not only unusual morphologies and particle characteristics but also some reported oxide formations on particle surfaces[9–12,23–26] in Nickel 718 and SS 316L. It should also be noted that the surface of the left particle in Figure 10 has an appearance of ridges or veins and is highly unusual compared with virgin GA powder observed in this study. The EDS images in Figure 10 clearly demonstrate areas of concentrated amounts of aluminum and oxygen on the 718 spatter particle surfaces and are consistent with recent reports of various oxide morphologies present[9–11] in analyzed spatter of similar alloy systems. While the most common spatter morphology found in this study was spherical dendritic surface particles, additional unique morphologies have been observed for Nickel 718 as demonstrated in Figure 11. This SEM image demonstrates a mixture of GA (bed) and process-generated particles and a typical mix of different morphologies. Figure 11 shows an organized pattern of spots on the particle surface and, the remaining images are EDS elemental maps of the spotted particle showing the spots to contain Al, Ti, and oxygen, consistent with those in Figure 10. It is expected that Al-rich and/or Ti-rich oxides would form in a low partial pressure oxygen environment in the machine chamber due to the alloy composition and favorable conditions for oxide formation. While a number of mechanisms for spot formation are suggested in recent literature, the varying oxide spots and film formations are most likely driven by the very high liquid temperature of the spatter generated by the AM process, either by liquid ejection or by particle entrainment, as the liquid travels through the chamber and solidifies.[13,26]

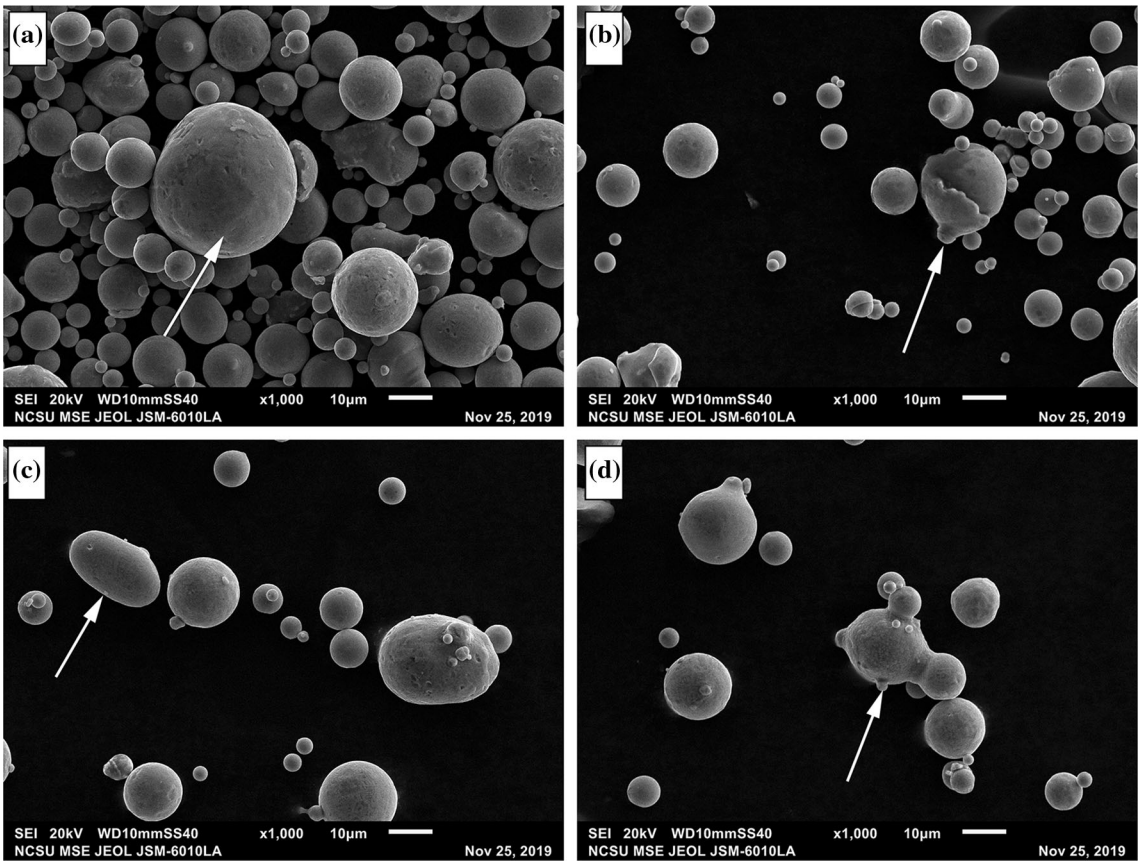

Fig. 7—SEM images of virgin GA ATI 718™ powder morphologies (*a*) spherical w/ typical surface, (*b*) particle with interacted liquid, (*c*) elongated particle, and (*d*) attached satellites. White arrows in the images indicate the specific feature(s) of interest.

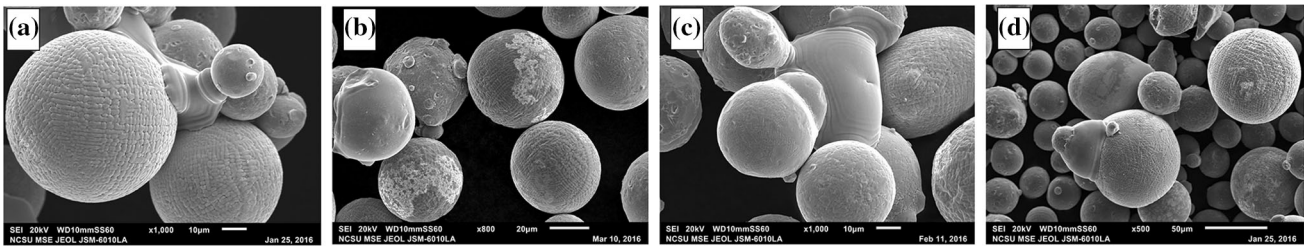

Fig. 8—SEM images of commonly seen morphologies in recycled 718 powder (*a*) spherical, dendritic, (*b*) dendritic, surface film, (*c*) agglomerated, and (*d*) combination particle.

To illustrate unusual morphologies such as the oxide spotting of spatter particles is not necessarily uncommon in PBF, or unique to Alloy 718, Figure 12 shows a montage of SEM spatter images for stainless steel 316L and Co28Cr6Mo in a similar laser PBF machine using standard OEM operating conditions. Elemental maps in Figure 12 show that 316L and Co28Cr6Mo spotted spatter particles have Si-Mn-rich oxides instead of the Al-Ti-rich oxides found in 718 spatter. These alloys have similar levels of favorable oxidizing residual elements (Al + Ti *vs* Si + Mn for 718, 316L & Co28Cr6Mo, respectively), and both alloys exhibit symmetrical and random oxide spotting. It should be noted that while the dislodged atomized bed particle component of spatter observed throughout the 718 study exhibited some surface films, discrete oxide droplets, and agglomeration, none of the dislodged particles were found to exhibit symmetrical or heavy oxide spotting. Also, most of the very heavily spotted particles were typically coarser than bed powder, indicating most likely these particles were from liquid generated during the PBF process, where these results are consistent with recent reports in 718 and 316L.[9–11,21,24–26] It is also logical that the increase in oxygen content in this study is heavily influenced by the presence of accumulating particles with films and spots which contain oxides.

An unplanned result that was observed during this study was the effect of recycling on magnetic behavior in 718. Typically, alloy 718 is non-magnetic to very low temperatures (< 20 K) where it then exhibits magnetic

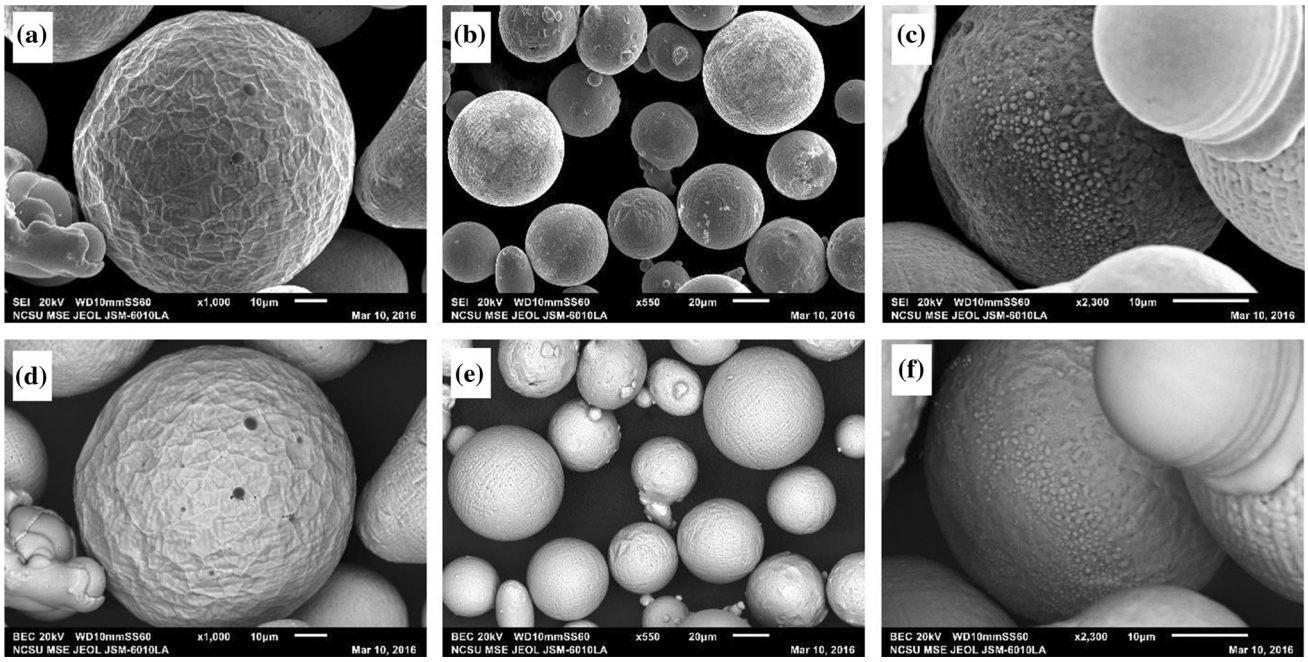

Fig. 9—SEM images of spatter with films and spots in SEI mode (*a*, *b*, *c*) and BEC mode (*d*, *e*, *f*) of a particle with deposits or spots (a, d), particles with surface films (b, e) and blisters on a particle (c, f).

susceptibility similar to a spin glass.[28] In the current study, post-build 718 powder was observed to exhibit magnetic characteristics. This was further analyzed on a Quantum Design SQUID MPMS3 instrument at room temperature to measure the magnetic coercivity of the − 140 mesh powder. Figure 13 shows the magnetic coercivity of − 140 mesh powder measured at different intervals over the course of the study. Figure 13(a) demonstrates that virgin atomized 718 powder shows no soft magnetic behavior; however, after 4, 7, and 10 builds, respectively, the powder shows increasing magnetic coercivity with increasing hysteresis in Figures 13(b) through (d). The reason for this is currently not understood but may be an effect of oxidation of particles after exposure to the laser and melt area oxidation of generated spatter particles. A recent report by Heiden *et al.* [10] demonstrated a similar effect in 316L where magnetic susceptibility increased in spatter, and a possible cause was attributed to the presence of single-phase ferrite, which was observed in some of the spatter particle population. However, no phase change was observed in the current study on alloy 718 and, the increase with magnetic coercivity is currently under study.

IV. CONCLUSIONS

Recycling 718 powder in a laser PBF system up to 10 times to build large articles caused a linear increase in particle size distribution, decrease in flowability, increase in oxygen content, and an increase in magnetic coercivity at room temperature in the powder feedstock after screening through a − 140 mesh screen after each build. Spatter particles accumulated in the feedstock over time exhibited morphologies quite different from the virgin gas-atomized powder. The spatter morphologies were observed consistently during the study and were classified into following categories: very spherical, dendritic, and satellite-free particles, highly agglomerated chains with liquid ligaments, particles with surface films, and typically larger particles with oxide-rich spots. The observed spots on the particles were found to be rich in aluminum, titanium, and oxygen and were distributed both randomly and symmetrically, respectively, across different particles. However, while oxygen content increased with each recycling event, no change in elemental majors was detected with ICP. The reused powder also had soft magnetic behavior at room temperature, which is highly uncommon for alloy 718 and is expected to be influenced by the presence of surface films and oxide spots observed in this study.

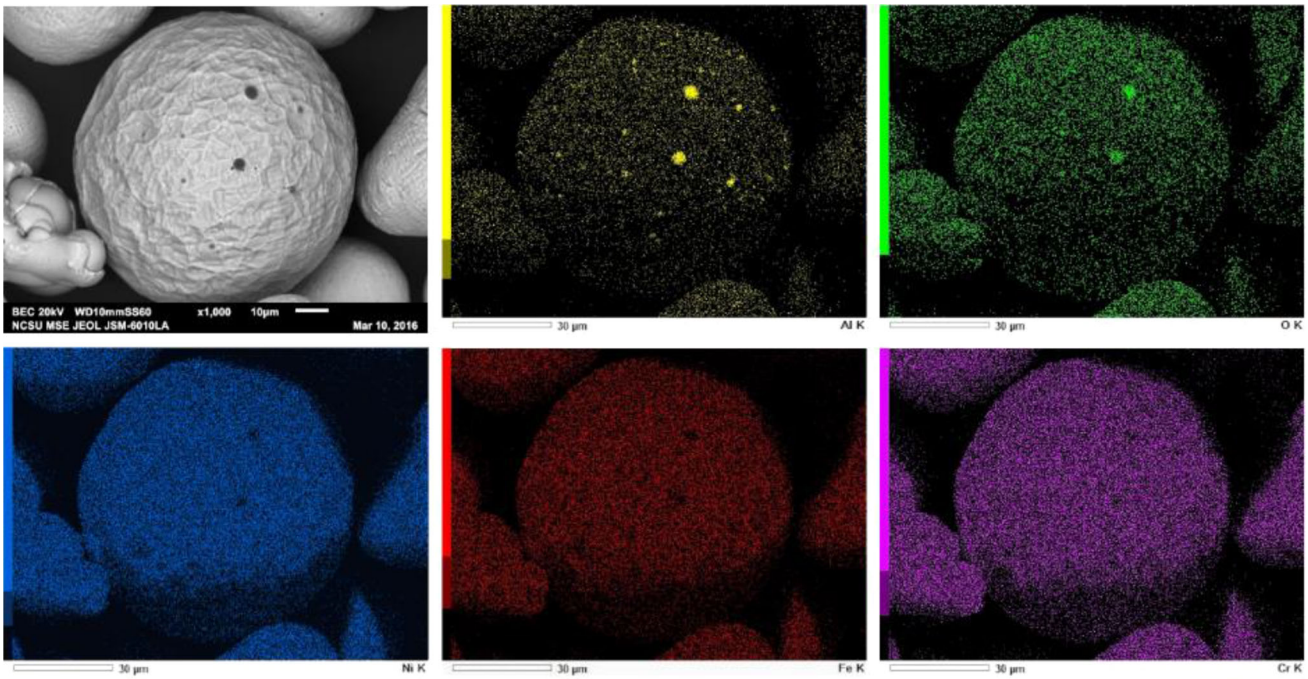

Fig. 10—SEM BEC of a spatter particle with surface spots and subsequent EDS elemental maps consisting of Al (yellow), oxygen (green), Ni (blue), Fe (red), and Cr (purple) (Color figure online).

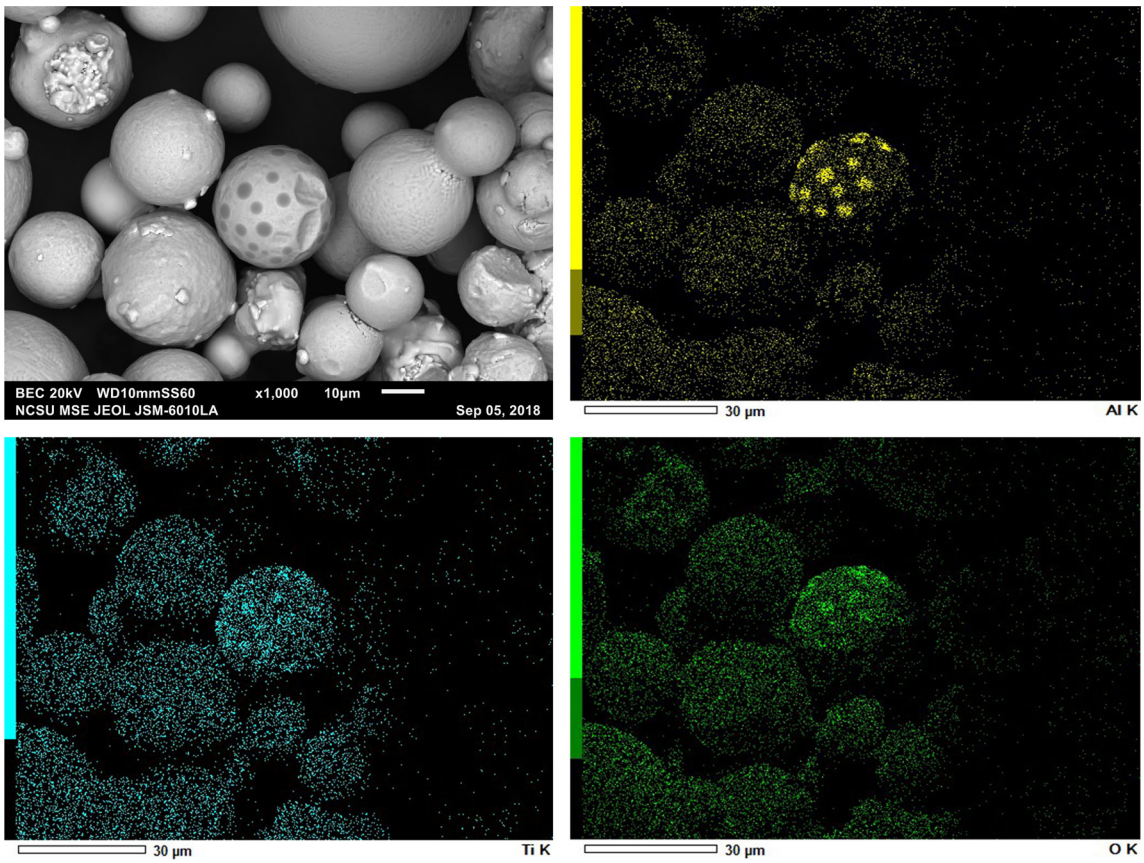

Fig. 11—EDS map of 718 spotted particle with Al (yellow), titanium (blue), and Oxygen (green) (Color figure online).

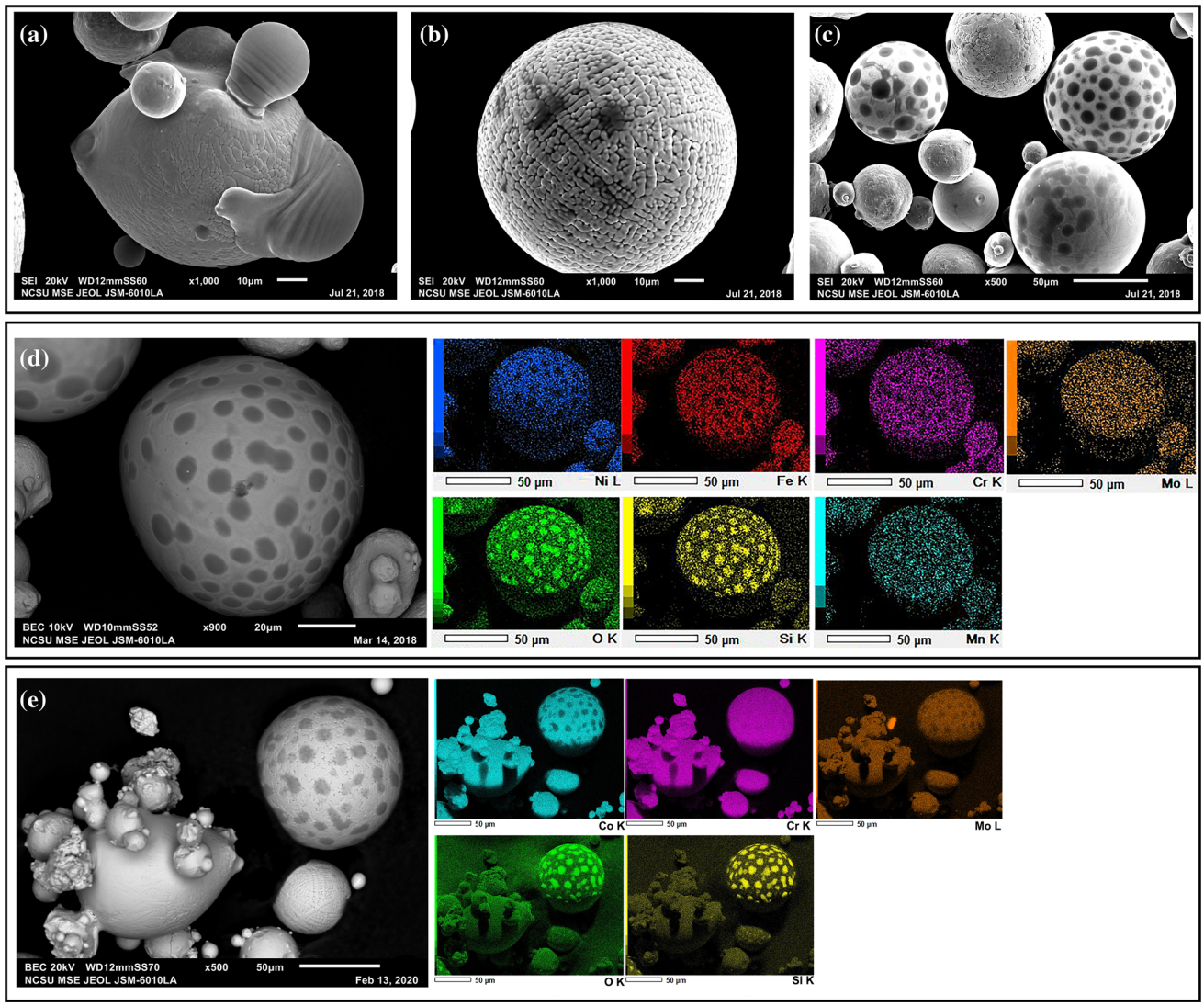

Fig. 12—Spatter morphologies observed from PBF of 316L (*a*) compression waves, agglomeration, (*b*) dendritic particle, (*c*) spotted particles, (*d*) EDS Map of 316L spotted spatter particles found in PBF, (*e*) EDS Map of Co28Cr6Mo spotted spatter particles found in PBF.

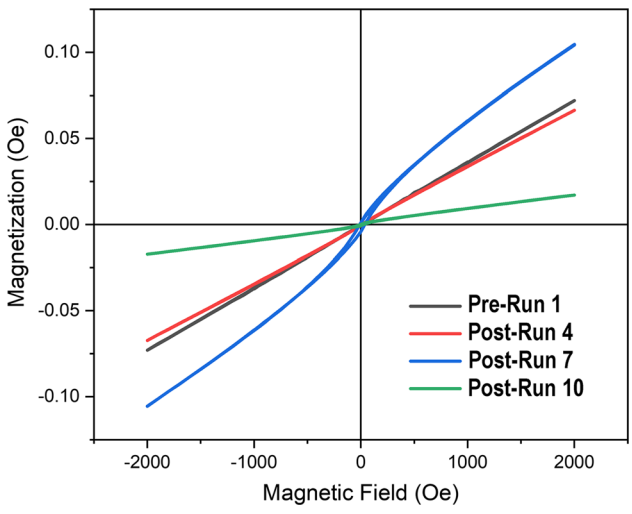

Fig. 13—Magnetic susceptibility of 718 powder measured at room temperature for powders before and after various stages of use.

ACKNOWLEDGMENTS

The authors would like to thank Allegheny Technologies Incorporated (ATI), Pittsburgh, PA, for supporting this project. This work was performed in part at the Analytical Instrumentation Facility (AIF) at North Carolina State University, which is supported by the State of North Carolina and the National Science Foundation (Award Number ECCS-1542015). The AIF is a member of the North Carolina Research Triangle Nanotechnology Network (RTNN), a site in the National Nanotechnology Coordinated Infrastructure (NNCI).

REFERENCES

1. M. Ruffo, C. Tuck, and R. Hague: *Proc. Inst. Mech. Eng. Part B*, 2006, vol. 220, pp. 1417–27.
2. W.J. Sames, F.A. List, S. Pannala, R.R. Dehoff, and S.S. Babu: *Int. Mater. Rev.*, 2016, vol. 61, pp. 315–60.

3. H.P. Tang, M. Qian, N. Liu, X.Z. Zhang, G.Y. Yang, and J. Wang: *JOM*, 2015, vol. 67, pp. 555–63.
4. P. Nandwana, W.H. Peter, R.R. Dehoff, L.E. Lowe, M.M. Kirka, F. Medina, and S.S. Babu: *Metall. Mater. Trans. B*, 2016, vol. 47B, pp. 754–62.
5. L.C. Ardila, F. Garciandia, J.B. González-Díaz, P. Álvarez, A. Echeverria, M.M. Petite, R. Deffley, and J. Ochoa: *Phys. Procedia*, 2014, vol. 56, pp. 99–107.
6. J.A. Slotwinski, E.J. Garboczi, P.E. Stutzman, C.F. Ferraris, S.S. Watson, and M.A. Peltz: *J. Res. Natl. Inst. Stand. Technol.*, 2014, vol. 119, pp. 460–93.
7. G. Jacob, C. Brown, A. Donmez, S. Watson, and J. Slotwinski: *NIST Advanced Manufacturing Series (NIST AMS) - 100-6*, February 2017.
8. A. Strondtl, O. Lyckfeldt, H. Brodin, and U. Ackelid: *JOM*, 2015, vol. 67, pp. 549–54.
9. M. Simonelli, C. Tuck, N.T. Aboulkhair, I. Maskery, I. Ashcroft, R.D. Wildman, and R. Hague: *Metall. Mater. Trans. A*, 2015, vol. 46A, pp. 3842–51.
10. M.J. Heiden, L.A. Deibler, J.M. Rodelas, J.R. Koepke, D.J. Tung, D.J. Saiz, and B.H. Jared: *Addit. Manuf.*, 2019, vol. 25, pp. 84–103.
11. A.N.D. Gasper, B. Szost, X. Wang, D. Johns, S. Sharma, A.T. Clare, and I.A. Ashcroft: *Addit. Manuf.*, 2018, vol. 24, pp. 446–56.
12. B. Sartin, T. Pond, B. Griffith, W, Everhart, L. Elder, E. Wenski, C. Cook, D. Wieliczka, W. King, A. Rubenchik, S. Wu, B. Brown, C. Johnson, and J. Crow: *Solid Freeform Fabr. Symp. Proc.*, 2017.
13. S. Ly, A.M. Rubenchik, S.A. Khairallah, G. Guss, and M.J.Matthews: *Sci. Rep.*, 2017, vol. 7, article no. 4085.
14. S.A. Khairallah, A.T. Anderson, A. Rubenchik, and W.E. King: *Acta Mater.*, 2016, vol. 108, pp. 36–45.
15. ASTM F3055-14a, *Additive Manufacturing Nickel Alloy (UNS N07718) with Powder Bed Fusion,* ASTM International, 2017.
16. ASTM F3184-16, *Additive Manufacturing Stainless Steel Alloy (UNS S31603) with Powder Bed Fusion,* ASTM International, 2017.
17. ASTM F75-18, *Standard Specification for Cobalt-28 Chromium-6 Molybdenum Alloy Castings and Casting Alloy for Surgical Implants (UNS R30075),* ASTM International, 2018.
18. P.A. Kulkarni, R.J. Berry, and M.S.A. Bradley: *Proc. Inst. Mech. Eng., Part E.*, 2010, vol. 224, pp. 159–68.
19. A. Lawley: *Atomization: The Production of Metal Powders (Monographs in P/m Series, No. 1),* Metal Powder Industries Federation, 1992.
20. R. German: *Powder Metallurgy and Particulate Materials Processing: The Processes, Materials, Products, Properties and Applications*, Metal Powder Industries Federation, 2005.
21. D. Wang, S. Wu, F. Fu, S. Mai, Y. Yang, Y. Liu, and C. Song: *Mater. Des.*, 2017, vol. 117, pp. 121–30.
22. A. Ladewig, G. Schlick, M. Fisser, V. Schulze, and U. Glatzel: *Addit. Manuf.*, 2016, vol. 10, pp. 1–9.
23. M.T. Andani, R. Dehghani, M.R. Karamooz-Ravari, R. Mirzaeifar, and J, Ni: *Mater. Des.*, 2017, vol. 131, pp. 460-9.
24. Y. Liu, Y. Yang, S. Mai, D. Wang, and C. Song: *Mater. Des.*, 2015, vol. 87, pp. 797–806.
25. R. Esmaeilizadeh, U. Ali, A. Keshavarzkermani, Y. Mahmoodkhani, E. Marzbanrad, and E. Toyserkani: *J. Manuf. Process.*, 2019, vol. 37, pp. 11–20.
26. C. Rock, R. Vadlakonda, S. Figurskey, C. Ledford, H. West, V. Miller, K. Daniels, T. Horn: *Addit. Manuf.*, 2020, article no. 101320.
27. V. Gunenthiram, P. Peyre, M. Schneider, M. Dal, C. Frédéric, and R. Fabbro: *J. Laser. Appl.*, 2017, vol. 29, article no. 022303.
28. I.B. Goldberg, M.R. Mitchell, A.R. Murphy, R.B. Goldfarb, and R.J. Loughran: *Magnetic Susceptibility of Inconel Alloys 718, 625, and 600 at Cryogenic Temperatures, Advances in Cryogenic Engineering Materials: Part A, edited by R. P. Reed and F. R. Fickett.* International Cryogenic Materials Conference Publication. Springer, Boston, 1990, pp. 755–62.

Publisher's Note Springer Nature remains neutral with regard to jurisdictional claims in published maps and institutional affiliations.